



High-performance BiVO₄ photoanodes cocatalyzed with an ultrathin α-Fe₂O₃ layer for photoelectrochemical application

Ligang Xia^a, Jing Bai^a, Jinhua Li^a, Qingyi Zeng^a, Linsen Li^a, Baoxue Zhou^{a,b,*}

^a School of Environmental Science and Engineering, Shanghai Jiao Tong University, No. 800 Dongchuan Rd., Shanghai, China

^b Key Laboratory of Thin Film and Microfabrication Technology, Ministry of Education, Shanghai 200240, China

ARTICLE INFO

Article history:

Received 3 August 2016

Received in revised form 3 November 2016

Accepted 9 November 2016

Available online 11 November 2016

Keywords:

BiVO₄ photoanode

Ultrathin α-Fe₂O₃ layer

Cocatalyst

Water splitting

Organic pollutant degradation

ABSTRACT

A high-performance bismuth vanadate (BiVO₄) photoanode cocatalyzed with an ultrathin α-Fe₂O₃ layer was fabricated for photoelectrochemical water splitting and organic pollutant degradation. The ultrathin α-Fe₂O₃ layer, which can facilitate the holes transfer to the surface efficiently and thus avoid high charge recombination, was deposited on the surface of the BiVO₄ photoanode using a spin-coating-based successive ionic layer adsorption and reaction (SILAR) method. The Fe₂O₃/BiVO₄ photoanode was characterized by various techniques, including X-ray diffraction, X-ray photoelectron spectroscopy, and scanning electron microscopy, while its photoelectrochemical activity was investigated by linear sweep voltammetry and incident photon-to-current conversion efficiency (IPCE). The optimized Fe₂O₃/BiVO₄ photoanode demonstrated a photocurrent density of 1.63 mA cm⁻² at 1.23 V vs. a reversible hydrogen electrode (RHE) in a 0.1 M KH₂PO₄ (pH 7) electrolyte under simulated AM1.5G solar light and an IPCE value above 27% at 400 nm, which were 2.14 times and triple that of pristine BiVO₄ photoanode, respectively. Furthermore, the Fe₂O₃/BiVO₄ photoanode showed excellent stability and efficiency for the photoelectrocatalytic degradation of phenol compared with the bare BiVO₄ photoanode. The chemical oxygen demand (COD) removal ratio increased from 42.3% to 68.89% after 120 min, which could be attributed to the efficient separation and transfer of the photogenerated carriers.

© 2016 Elsevier B.V. All rights reserved.

1. Introduction

With the development of modern society, energy shortage and environmental pollution are urgent issues that need resolution. Following the pioneering work of Fujishima and Honda [1,2], photoelectrochemical (PEC) techniques have been developed to address the above problems using sunlight to split water and degrade organic pollutants [3].

One key technical problem encountered in PEC applications is the development of a high quantum efficiency and visible light responsive photoelectrode material which plays an important role in the PEC conversion of solar energy to chemical energy in water splitting and waste water treatment [4–6]. Among the various photoelectrodes studied in PEC applications, monoclinic bismuth vanadate (BiVO₄) has been identified as one of the most promising n-type semiconductor photoanodes for water splitting and organic pollutant degradation. Its small bandgap (*i.e.* 2.4 eV) allows significant visible light absorption and its positive valence band edge

(*i.e.* 2.4 V vs. RHE) provides a sufficient overpotential for water and organic oxidation [7,8]. However, the PEC activity of unmodified BiVO₄ is still limited by a number of factors, including excessive charge recombination, poor charge transport properties, and poor water oxidation kinetics. To address these limitations, various strategies have been developed to improve the PEC properties of BiVO₄ photoanode, including the incorporation of W and Mo into BiVO₄ to enhance conductivity and hole diffusion length [9–11], the integration of BiVO₄ with other semiconductors to create heterojunction structure to promote charge separation [12–16], and decoration of the BiVO₄ surface with a cocatalyst such as Co, Eu₂O₃, and RhO₂ to facilitate the oxygen evolution reaction [17–19].

Fe₂O₃, composed of the most abundant transition metal and oxygen, possesses the advantages of low cost and environmental friendliness. In addition, the energy level of Fe₂O₃ is compatible with that of BiVO₄ (Fig. 1). However, to date, Fe₂O₃ cocatalyzed BiVO₄ photoanodes have received little attention. As can be seen from Fig. 1, the BiVO₄ valence band edge is obviously below the Fe₂O₃ band edge at pH 7, which satisfies the energetic requirement for hole transfer. Moreover, the Fermi level of BiVO₄ is higher than that of Fe₂O₃; hence, for contact formation, the electrons will be transferred from the BiVO₄ to Fe₂O₃ until a thermodynamic

* Corresponding author. Tel.: +86 21 5474 7351; fax: +86 21 5474 7351.

E-mail address: zhoubaoxue@sjtu.edu.cn (B. Zhou).

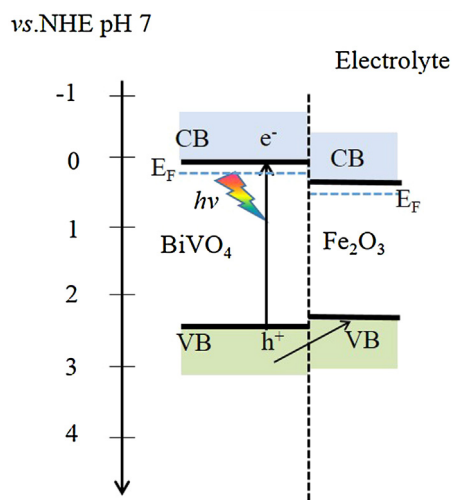


Fig. 1. The deduced relative band positions of Fe_2O_3 and BiVO_4 (data from Ref. [20]).

equilibrium is established. This will result in the formation of an electron depletion region and surface upward-bent band in BiVO_4 to facilitate hole transfer.

However, the thickness of Fe_2O_3 layer on the surface of BiVO_4 would be a key factor to restrict the improvement of PEC properties since Fe_2O_3 has a short carrier diffusion length and low conductivity [21,22]. Although BiVO_4 powder modified by Fe_2O_3 achieved an improvement in photocatalytic activity [23], the thickness of Fe_2O_3 layer on the surface of BiVO_4 should be controlled appropriately so as to transfer the holes from BiVO_4 to the surface quickly. Based on this, an ultrathin $\alpha\text{-Fe}_2\text{O}_3$ layer cocatalyzed BiVO_4 photoanode was designed and fabricated using a spin-coating-based successive ionic layer adsorption and reaction (SILAR) method in this paper. The ultrathin $\alpha\text{-Fe}_2\text{O}_3$ layer modified BiVO_4 photoanode exhibited excellent stability and highly efficient performance of water oxidation and organic pollutants degradation.

2. Experimental section

2.1. Preparation of BiVO_4 photoelectrode

First, a precursor solution containing 0.3 M bismuth and vanadium was prepared by dissolving bismuth nitrate pentahydrate and ammonium metavanadate in 2 M nitric acid aqueous solution. Then, the precursor solution was spin coated on a fluorine-doped tin oxide (FTO) glass substrate to produce the BiVO_4 photoelectrode. For each layer of coating, the sample was annealed in air at 450°C for 20 min on a hot plate. The last step was to anneal the samples at 450°C in a furnace for 3 h with heating and cooling rates of $1^\circ\text{C}/\text{min}$.

2.2. Preparation of $\text{Fe}_2\text{O}_3/\text{BiVO}_4$ photoelectrode

The $\text{Fe}_2\text{O}_3/\text{BiVO}_4$ photoelectrode was fabricated using the spin-coating-based successive ionic layer adsorption and reaction (SILAR) method. First, 0.1 M $\text{Fe}(\text{NO}_3)_3 \cdot 9\text{H}_2\text{O}$ and 0.1 M NaOH aqueous solutions were prepared. Then, these two solutions were spin coated on the BiVO_4 photoelectrode in sequence. For each layer of coating, the sample was dried in air and then annealed at 450°C in a furnace for 2 h with heating and cooling rates of $1^\circ\text{C}/\text{min}$. The resulting photoanodes are denoted as $n\text{-Fe}_2\text{O}_3/\text{BiVO}_4$ (n corresponds to the number of coating layers).

2.3. Preparation of Fe_2O_3 powder

$\text{Fe}(\text{NO}_3)_3 \cdot 9\text{H}_2\text{O}$ (0.1 M) and NaOH (0.1 M) aqueous solutions were mixed with the same volume ratio and then evaporated. Afterwards, the resulting solid powder was annealed at 450°C in a furnace for 2 h with heating and cooling rates of $1^\circ\text{C}/\text{min}$. The final product was centrifuged, washed several times with de-ionized water, and dried in air.

2.4. Characterization of photoelectrodes

The morphologies of the samples were studied using a field emission scanning electron microscope (Nova NanoSEM NPE218). XPS was conducted using an AXIS Ultra DLD instrument (Kratos, Shimadzu) with non-chromatic $\text{Al K}\alpha$ radiation at 12 kV and 25 mA. X-ray diffractometry (XRD; AXS-8 Advance, Bruker, Germany) was used to determine the crystal phase of the prepared samples. The UV–vis absorption spectra of the samples were scanned on a UV–vis spectrophotometer (TU-1901, Beijing Purkinje General Instrument Co.).

2.5. Photoelectrochemical property tests

The Incident photon-to-charge conversion efficiency (IPCE) was measured using a monochromator (Zolix, China), 500 W xenon arc lamp, calibrated silicon photodetector and power meter. The PEC tests were controlled from an electrochemical workstation (CHI 660c, CH Instruments Inc., USA). A 350 W xenon lamp (Shanghai Hualun Bulb Factory) was used as a simulated solar light source, and without further description, all experiments were carried out under AM1.5G (light density, 100 mW cm^{-2}) solar light illumination. The linear sweep voltammogram (LSV) of the photoelectrodes was tested in 0.1 M KH_2PO_4 (pH 7) electrolyte solution using a three-electrode system including a platinum foil counter electrode, Ag/AgCl reference and the prepared photoelectrode as the working electrode. The organic compound degradation experiments were performed under the following conditions: moderate stirring, 0.6 V (vs. Ag/AgCl) applied bias, 0.1 mol L^{-1} sodium sulfate electrolyte, 25 mL reaction solution. Chemical oxygen demand (COD) of phenol was determined using the methods reported in the literatures [24,25]. All runs were repeated at least three times to check the reproducibility.

3. Results and discussion

3.1. The characterization of bare BiVO_4 and $\text{Fe}_2\text{O}_3/\text{BiVO}_4$ photoanode

The morphologies of the prepared BiVO_4 and $3\text{-Fe}_2\text{O}_3/\text{BiVO}_4$ photoanodes were investigated using scanning electron microscopy (Fig. 2). The surface of the bare BiVO_4 photoanode consisted of small crystal grains tens of nanometers (Fig. 2a). After Fe_2O_3 deposition, the grain boundary of BiVO_4 became obscure and its surface was covered by a thin Fe_2O_3 layer (Fig. 2b). The cross sectional SEM in the inset shows a well-connected BiVO_4 layer of approximately 180 nm thick with an increase in film thickness to 192 nm after deposition of the Fe_2O_3 layer. Inductively coupled plasma optical emission spectrometry (ICP-OES) measurements indicated that the Fe_2O_3 loading was $\sim 4.1 \text{ wt}\%$. Fig. 2c–f shows the element mapping Bi, V, O and Fe, respectively, suggesting the presence of Fe on the BiVO_4 surface. Fig. 2g shows XRD diffraction patterns of BiVO_4 and $\text{Fe}_2\text{O}_3/\text{BiVO}_4$ photoanodes. The experiments confirmed that both BiVO_4 photoanodes have a single monoclinic scheelite structure according to the standard card of BiVO_4 (JCPDS 14-0688) [26]. However, the diffraction phase of Fe oxide species could not be determined from the XRD

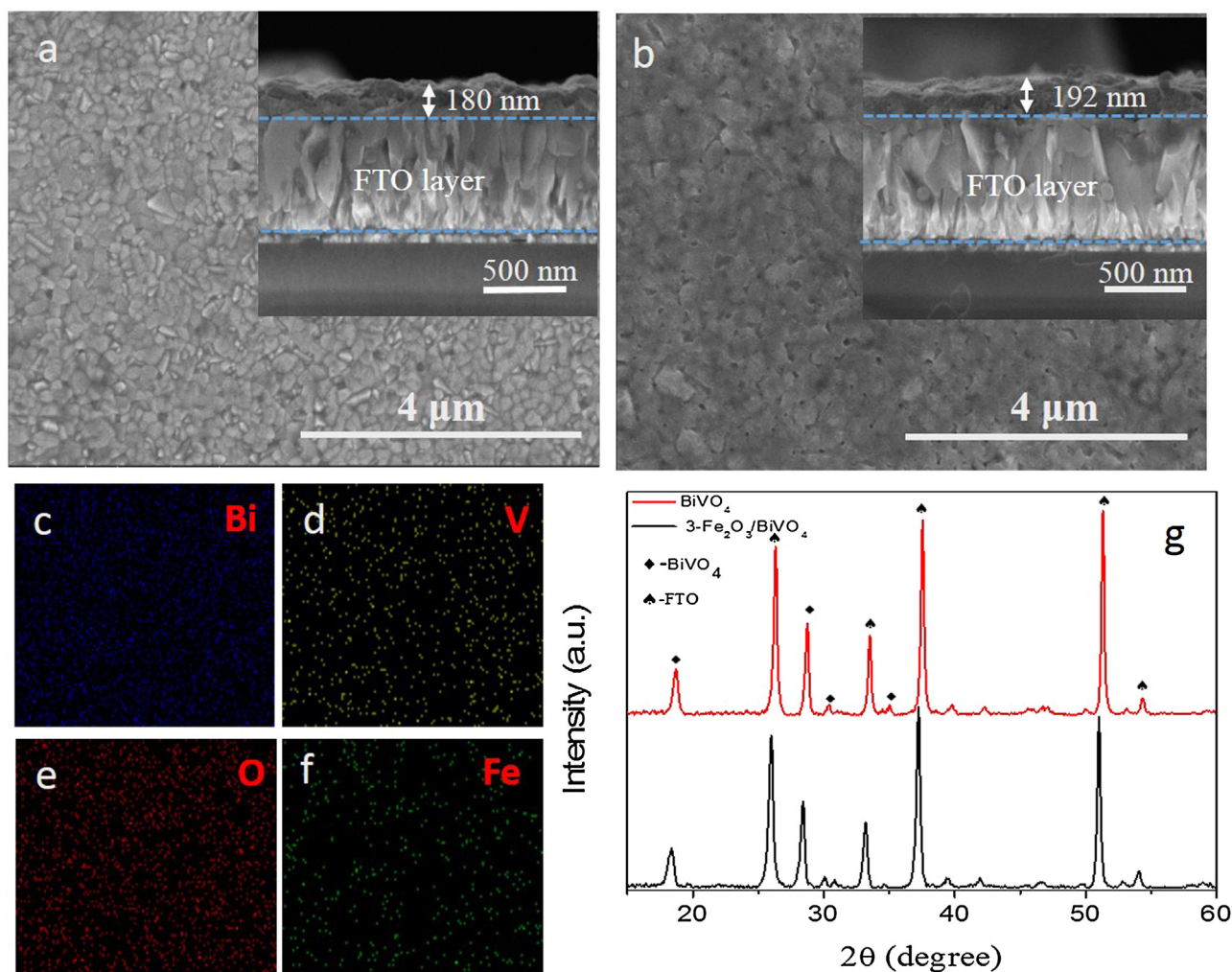


Fig. 2. Top-view SEM images of (a) bare BiVO₄, (b) 3-Fe₂O₃/BiVO₄ photoanodes (Insets are the corresponding cross sectional SEM images). (c–f) The corresponding STEM-EDS elemental mapping images of Bi, V, O and Fe, respectively and (g) XRD patterns of bare BiVO₄ and Fe₂O₃/BiVO₄ photoanodes.

diffraction patterns. This may be due to the low content of Fe oxide species below the detection limit of the XRD analysis.

To confirm the physicochemical states of Fe on the BiVO₄ surface, XPS analysis was conducted, as shown in Fig. 3. Peaks with binding energies of 158.6 and 164.4 eV were assigned to Bi³⁺ 4f_{7/2} and Bi³⁺ 4f_{5/2} in the 3-Fe₂O₃/BiVO₄ (Fig. 3) and BiVO₄ (Fig. S1) photoanodes [27], respectively. In addition, based on a previous literature report, the V 2p binding energy (*i.e.*, 516.7 eV) corresponded to V⁵⁺ in BiVO₄ [28]. Furthermore, no peaks corresponding to Fe 2p were visible in the spectrum of BiVO₄, while peaks with binding energies of 711 and 724.2 eV in the 3-Fe₂O₃/BiVO₄ photoanode corresponded to Fe 2p_{3/2} and Fe 2p_{1/2}, respectively. Indeed, this is characteristic of the Fe³⁺ present in Fe₂O₃ [23,29]. A characteristic satellite peak corresponding to α-Fe₂O₃ also appeared at 718.8 eV [30]. Moreover, peaks at 529.8 and 532.3 eV in both the BiVO₄ and 3-Fe₂O₃/BiVO₄ photoanodes corresponded to O 1s and were assigned to the lattice oxygen atoms in BiVO₄ or Fe₂O₃ and adsorbed water [31], respectively. An XRD pattern of Fe₂O₃ powder was also collected to accurately determine the crystal type of Fe₂O₃. Fig. 4 shows that all of the diffraction peaks correspond to hematite (α-Fe₂O₃).

Fig. 5 shows the UV–vis absorption spectra of the BiVO₄ and 3-Fe₂O₃/BiVO₄ photoanodes. No obvious differences are observed except that the Fe₂O₃/BiVO₄ photoanode displays slightly higher absorption in both UV and visible light regions than the BiVO₄

photoanode, which could be attributed to the larger absorption coefficient and narrower band gap of Fe₂O₃ [32]. As determined from their corresponding (αhν)² versus hν plots (Fig. S2), both photoanodes exhibited an E_g of 2.55 eV.

3.2. Photoelectrochemical properties of bare BiVO₄ and Fe₂O₃/BiVO₄ photoanodes

Fig. 6 shows that both BiVO₄ and Fe₂O₃/BiVO₄ photoanodes generate anodic photocurrent in 0.1 M KH₂PO₄ under solar simulated illumination (AM 1.5G, 100 mW cm⁻²). Compared to pristine BiVO₄, the onset potential of Fe₂O₃/BiVO₄ photoanode is significantly reduced with a distinct cathodic shift. The bare BiVO₄ photoanode showed a photocurrent density of 0.76 mA cm⁻² at 0.6 V vs. Ag/AgCl. Hereafter, the photocurrent density will be compared at this potential, the standard reversible potential for water oxidation. The 3-Fe₂O₃/BiVO₄ photoanode showed the highest photocurrent density of 1.63 mA cm⁻², or approximately 2.14 times that of bare BiVO₄ and was superior to those of similar systems including Fe₂O₃/3DOM-BiVO₄ (0.16 mA cm⁻²) [33], WO₃ (0.72 mA cm⁻²) [34], BiVO₄ (0.76 mA cm⁻²), and α-Fe₂O₃ (0.13 mA cm⁻²), which was prepared according to Ref. [29] when tested in 0.1 M KH₂PO₄. The significant improvement in photocurrents clearly reveals enhanced PEC activity upon Fe₂O₃ loading. The Fe₂O₃ layers were deposited by the SILAR method. The deposited layer of Fe₂O₃ was opti-

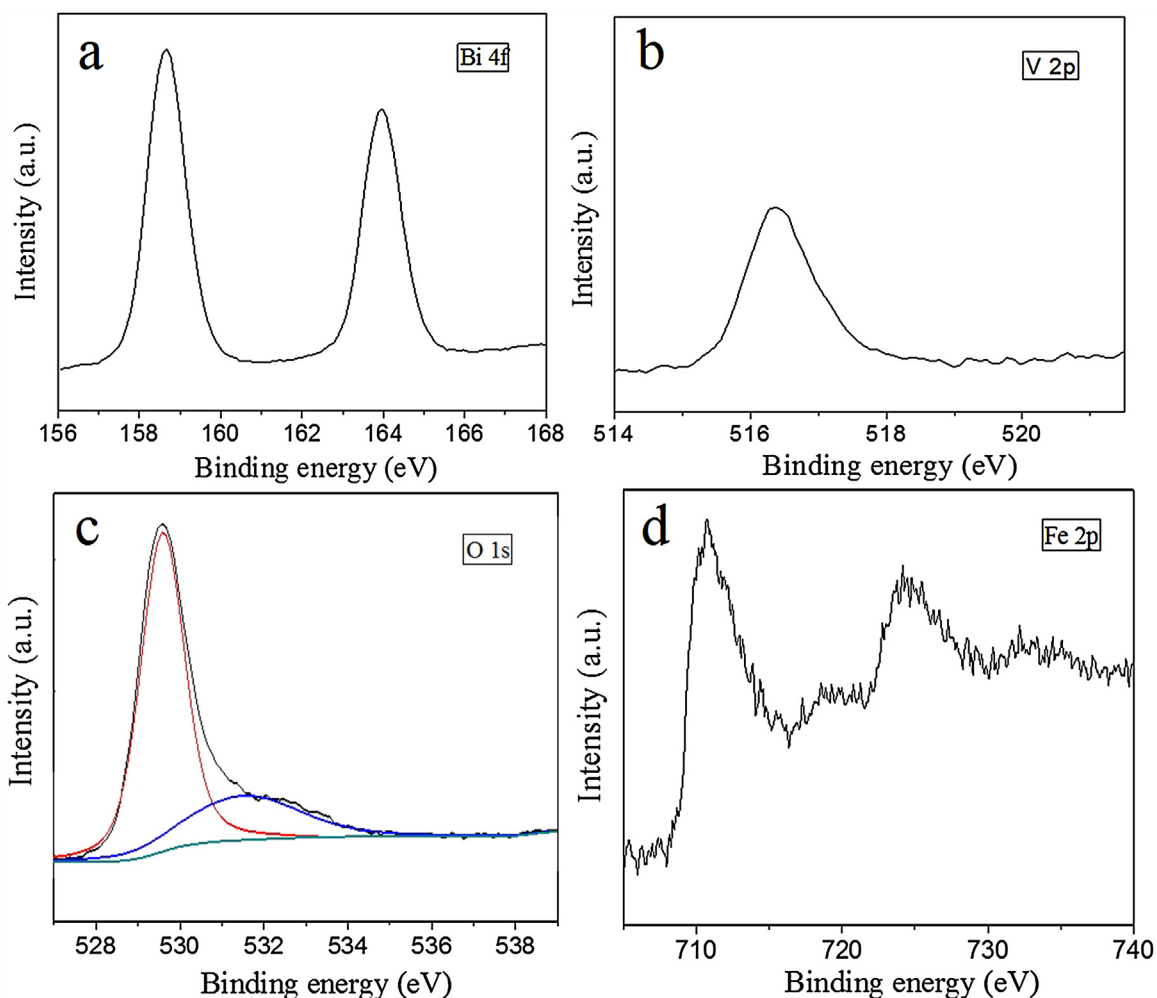


Fig. 3. (a) Bi 4f, (b) V 2p, (c) O 1s, and (d) Fe 2p X-ray photoelectron spectra for the 3-Fe₂O₃/BiVO₄ photoanode.

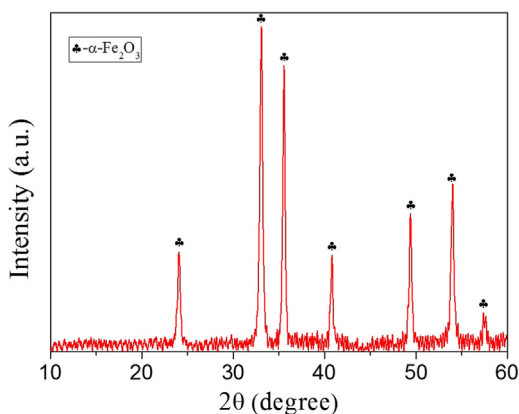


Fig. 4. XRD pattern of the Fe₂O₃ powder.

mized for the highest photocurrent generation, as shown in Fig. 6a. As the number of layers increased, the photocurrent density initially increased, but then began to decrease once again. The initial increase was attributed to an increase in the number of catalytically active sites upon increasing the number of Fe₂O₃ layers, resulting in an increase in photocurrent density. However, beyond the optimal point, a further increase in thickness of the Fe₂O₃ layer resulted in an increase in the equivalent bulk resistance because of the short carrier diffusion length and low conductivity of Fe₂O₃

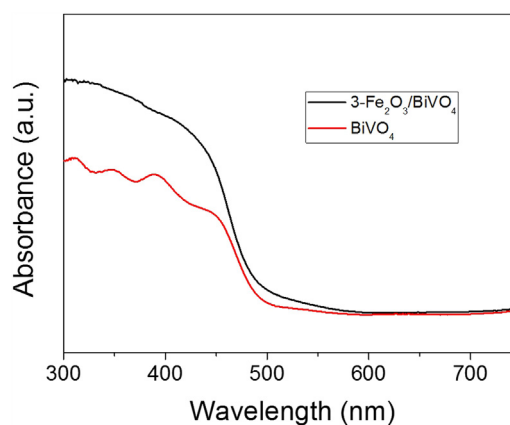


Fig. 5. UV-vis absorption spectra of bare BiVO₄ and Fe₂O₃/BiVO₄ photoanodes.

[21,22], thereby resulting in a decreased photocurrent density. This allowed us to conclude that the optimal thickness was obtained using 3 layers of Fe₂O₃, which could be estimated as a thickness of 12 nm from Fig. 2.

According to Fig. 6b, the onset potentials of the BiVO₄, 3-Fe₂O₃/BiVO₄, 5-Fe₂O₃/BiVO₄, and 7-Fe₂O₃/BiVO₄ photoanodes for water oxidation were 1.616, 1.266, 1.236, and 1.209 V (vs. Ag/AgCl, at $j=0.1 \text{ mA cm}^{-2}$), respectively. As the theoretical value of the water oxidation potential is 1.23 V (vs. RHE), in the neutral envi-

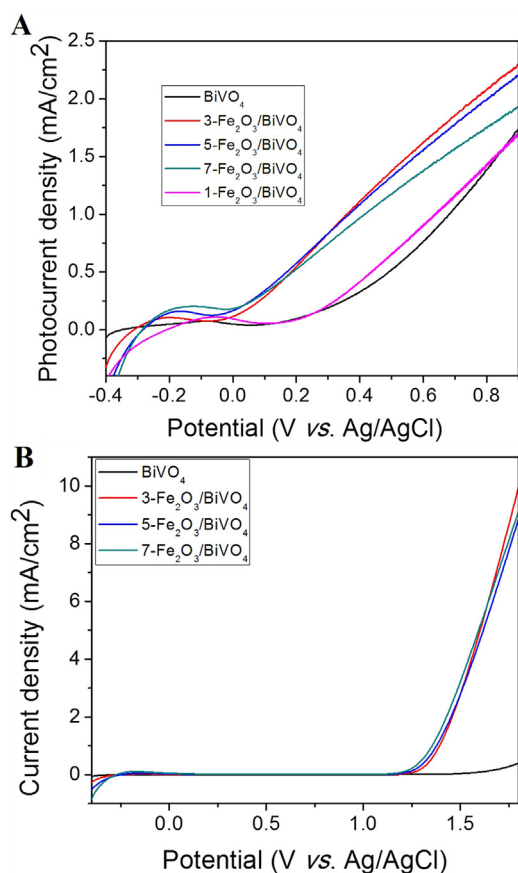


Fig. 6. *J*-*V* curves of different photoanodes measured (A) with and (B) without AM 1.5G illumination (100 mW cm^{-2}) for water oxidation.

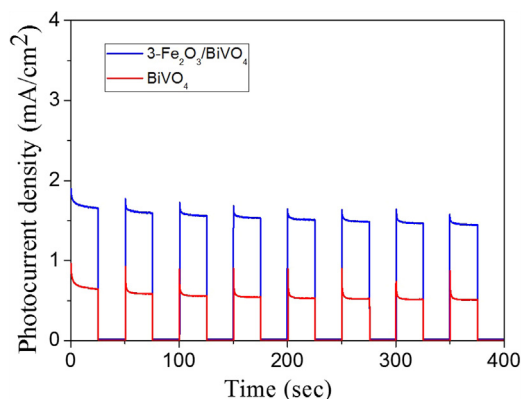


Fig. 7. Transient photocurrents of $\text{Fe}_2\text{O}_3/\text{BiVO}_4$ and BiVO_4 photoanodes in phosphate buffer solution (pH 7) under AM1.5G illumination.

ronment examined herein, the overpotentials for water oxidation using the above photoelectrodes were 996, 646, 616, and 589 mV, respectively. Thus, the clear cathodic shifts in the onset potentials and overpotentials for water oxidation compared to the pristine BiVO_4 indicate the catalytic effect of Fe_2O_3 [35,36]. Because of the poor water oxidation kinetics of BiVO_4 , the photogenerated holes accumulated on the photoanode surface result in significant surface charge recombination. Fe_2O_3 loading could significantly reduce the amount of accumulated holes and thus prohibit surface recombination during water oxidation, as shown by the much less pronounced photocurrent transients (Fig. 7).

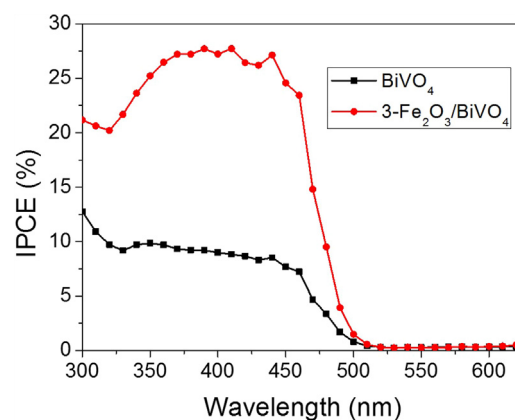


Fig. 8. IPCE plots of bare BiVO_4 and $\text{Fe}_2\text{O}_3/\text{BiVO}_4$ photoanodes measured at 1.23 V vs. RHE in 0.1 M KH_2PO_4 (pH 7).

The IPCE was calculated by measuring the photocurrent under monochromatic light at 1.23 V vs. RHE according to the following equation [37,38]:

$$\text{IPCE}(\%) = (1240 \times I) / (\lambda \times J_{\text{light}})$$

where I is the photocurrent density, λ is the incident light wavelength, and J_{light} is the measured irradiance. The IPCE values of BiVO_4 and $3\text{-Fe}_2\text{O}_3/\text{BiVO}_4$ photoanodes at 400 nm are approximately 9% and 27.2%, respectively (Fig. 8). The improved IPCE value of BiVO_4 after Fe_2O_3 modification demonstrates that the $\text{Fe}_2\text{O}_3/\text{BiVO}_4$ photoanode has successfully transformed the photo-generated electrons and holes to the photoelectrochemical water oxidation activity with much less efficiency loss.

In addition to a high PEC activity, the stability of the photoelectrode is also essential for successful PEC application. Thus, to probe the durability of the various photoelectrodes under constant working conditions, the long-term stabilities of the photocurrent densities as a function of time were measured, as shown in Fig. S3. The photocurrent density of the $3\text{-Fe}_2\text{O}_3/\text{BiVO}_4$ photoanode decreased from 1.62 to 1.49 mA cm^{-2} , while that of the BiVO_4 photoanode decreased from 0.72 to 0.46 mA cm^{-2} . In addition, the $3\text{-Fe}_2\text{O}_3/\text{BiVO}_4$ and BiVO_4 films decayed by ~8% and 36.1%, respectively. These results indicate that $\text{Fe}_2\text{O}_3/\text{BiVO}_4$ is sufficiently stable for use in PEC applications likely due to the ultrathin Fe_2O_3 film retarding the formation of Bi, and thus preventing the photocorrosion of BiVO_4 photoanode. Furthermore, the variation in gas evolution with time from the $3\text{-Fe}_2\text{O}_3/\text{BiVO}_4$ and BiVO_4 photoelectrodes (Fig. S4) demonstrated that the O_2 and H_2 evolution rates for $3\text{-Fe}_2\text{O}_3/\text{BiVO}_4$ were approximately 13.53 and $27.47 \mu\text{mol cm}^{-2} \text{ h}^{-1}$, respectively, which were superior to those of the pristine BiVO_4 photoanode.

To demonstrate the improved photoactivity of the $\text{Fe}_2\text{O}_3/\text{BiVO}_4$ photoanode for organic pollutant degradation, we conducted photocatalytic degradation experiments using phenol, a typical colorless contaminant in industrial wastewater. The chemical oxygen demand (COD) was tested to evaluate the degree of degradation or mineralization of the organic species, since decolorization could not reveal information regarding mineralization. The variation in the COD of aqueous solutions of phenol (50 mg/L) with irradiation time using the BiVO_4 and $\text{Fe}_2\text{O}_3/\text{BiVO}_4$ photoanodes is shown in Fig. 9. Indeed, the $\text{Fe}_2\text{O}_3/\text{BiVO}_4$ photoanode exhibited excellent photocatalytic activity for phenol degradation, with a decrease in the COD value from 118.3 to 36.8 mg/L after 120 min. This corresponded to a superior 68.89% COD removal ratio for the $\text{Fe}_2\text{O}_3/\text{BiVO}_4$ photoanode compared to 42.3% for the pristine BiVO_4 photoanode.

A schematic description of the mechanism for both the PEC degradation of phenol and the splitting of water in an $\text{Fe}_2\text{O}_3/\text{BiVO}_4$

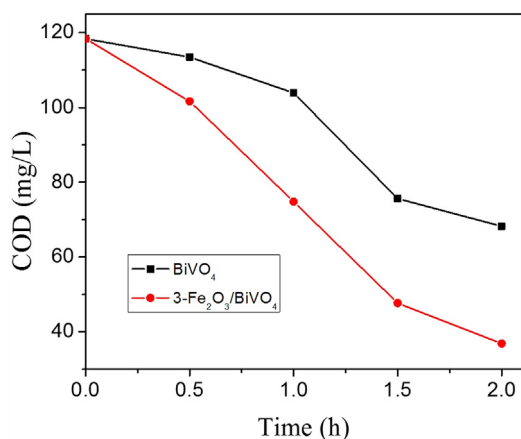
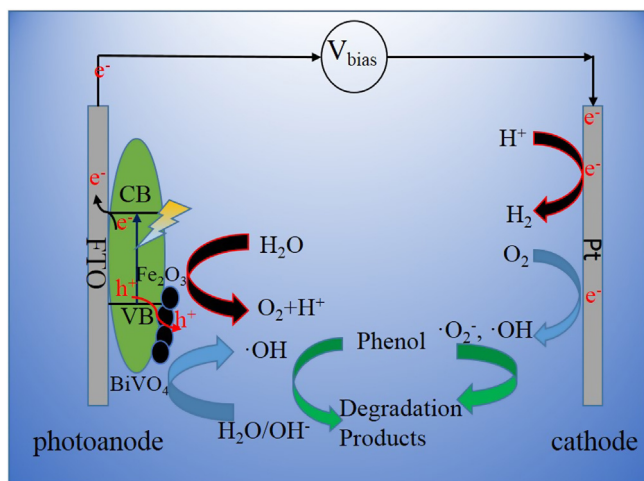


Fig. 9. Variation in the COD of aqueous phenol solutions (50 mg/L) with irradiation time using the pristine BiVO₄ and 3-Fe₂O₃/BiVO₄ photoanodes.



Scheme 1. A schematic illustration of charge separation and transfer in the Fe₂O₃/BiVO₄ photoanode system during PEC degradation and water splitting under light irradiation.

photoanode system is illustrated in Scheme 1. Due to the presence of the oxidation co-catalyst Fe₂O₃ thin film of the composite photoanode, the strong oxidative power of holes (h⁺) (+2.4 V vs. RHE) generated in the valence band of BiVO₄ upon light irradiation can be efficiently transferred to surface-adsorbed water and hydroxyl groups to generate •OH radicals. In contrast, when an appropriate bias potential was applied to the Fe₂O₃/BiVO₄ photoanode, photo-generated electrons efficiently move to the external circuit so that •O₂^{•−} can readily form on the cathode. As a result, the simultaneous existence of an external bias and Fe₂O₃ oxidation cocatalyst benefits the efficient separation and transfer of the photo-excited electrons and holes and thus effectively improves the degradation efficiency. With regards to water splitting, the ultrathin Fe₂O₃ film dramatically reduces the over potential and the strong oxidative power of the holes (h⁺) generated in BiVO₄ valence band upon light irradiation are efficiently transferred to Fe₂O₃ surface-adsorbed water to produce oxygen. Meanwhile, the electrons are transported to the Pt cathode where hydrogen is produced.

4. Conclusions

In summary, a high-performance bismuth vanadate (BiVO₄) photoanode cocatalyzed with an ultrathin α-Fe₂O₃ layer for photoelectrochemical water splitting and organic pollutant degra-

dation is presented. The photocurrent density of the optimized Fe₂O₃/BiVO₄ increased approximately 114.5% from that of pristine BiVO₄ and its incident photon conversion efficiency was also greatly improved. It was demonstrated that the existence of a thin Fe₂O₃ co-catalyst reduced the accumulation of holes on the surface and thus reduced charge recombination. The optimized Fe₂O₃/BiVO₄ photoanode also showed excellent stability and degradation efficiency for PEC degradation of phenol in a neutral aqueous solution.

Acknowledgements

The authors are grateful for financial support provided by the National Nature Science Foundation of China (No. 21576162, No. 51578332, No. 21507085, and No. 21276153) and the Shanghai Yangfan Program (14YF1401500).

Appendix A. Supplementary data

Supplementary data associated with this article can be found, in the online version, at <http://dx.doi.org/10.1016/j.apcatb.2016.11.015>.

References

- [1] A. Fujishima, K. Honda, *Nature* 238 (1972) 37–38.
- [2] C.-C. Wang, J.-R. Li, X.-L. Lv, Y.-Q. Zhang, G. Guo, *Energy Environ. Sci.* 7 (2014) 2831–2867.
- [3] X. Chen, S. Shen, L. Guo, S.S. Mao, *Chem. Rev.* 110 (2010) 6503–6570.
- [4] X. Chen, L. Liu, P.Y. Yu, S.S. Mao, *Science* 331 (2011) 746–750.
- [5] D. Wang, X. Zhang, P. Sun, S. Lu, L. Wang, Y. Wei, Y. Liu, *Int. J. Hydrogen Energy* 39 (2014) 16212–16219.
- [6] Q. Chen, J. Li, X. Li, K. Huang, B. Zhou, W. Shangguan, *ChemSusChem* 6 (2013) 1276–1281.
- [7] Y. Park, K.J. McDonald, K.S. Choi, *Chem. Soc. Rev.* 42 (2013) 2321–2327.
- [8] S.K. Pillai, T.E. Furtak, L.D. Brown, T.G. Deutsch, J.A. Turner, A.M. Herring, *Energy Environ. Sci.* 4 (2011) 5028–5034.
- [9] X. Zhang, X. Quan, S. Chen, Y. Zhang, J. Hazard. Mater. 177 (2010) 914–917.
- [10] M. Li, L. Zhao, L. Guo, *Int. J. Hydrogen Energy* 35 (2010) 7127–7133.
- [11] W. Yao, H. Iwai, J. Ye, *Dalton Trans.* 252 (2008) 1426–1430.
- [12] Ho-Kimura, S.J.A. Moniz, A.D. Handoko, J. Tang, J. Mater. Chem. A 2 (2014) 3948–3953.
- [13] F.F. Abdi, R. van de Krol, *J. Phys. Chem. C* 116 (2012) 9398–9404.
- [14] S.J.A. Moniz, J. Zhu, J. Tang, *Adv. Energy Mater.* 4 (2014) 1301590.
- [15] L. Zhang, E. Reisner, J.J. Baumberg, *Energy Environ. Sci.* 7 (2014) 1402–1408.
- [16] J.H. Kim, G. Magesh, H.J. Kang, M. Banu, J.H. Kim, J. Lee, J.S. Lee, *Nano Energy* 15 (2015) 153–163.
- [17] S. Xie, W. Wei, S. Huang, M. Li, P. Fang, X. Lu, Y. Tong, *J. Power Sources* 297 (2015) 9–15.
- [18] F. Lin, D.E. Wang, Z.X. Jiang, Y. Ma, J. Li, R.G. Li, C. Li, *Energy Environ. Sci.* 5 (2012) 6400–6406.
- [19] Y. Zhang, D. Wang, X. Zhang, Y. Chen, L. Kong, P. Chen, Y. Wang, C. Wang, L. Wang, Y. Liu, *Electrochim. Acta* 195 (2016) 51–58.
- [20] S.J.A. Moniz, S.A. Shevlin, D.J. Martin, Z. Guo, J. Tang, *Energy Environ. Sci.* 8 (2015) 731–759.
- [21] F.L. Formai, S.R. Pendlebury, M. Cornuz, S.D. Tilley, M. Gratzel, J.R. Durrant, *J. Am. Chem. Soc.* 136 (2014) 2564–2574.
- [22] M. Forster, R.J. Potter, Y. Ling, Y. Yang, D.R. Klug, Y. Li, A.J. Cowan, *Chem. Sci.* 6 (2015) 4009–4016.
- [23] P. Cai, S. Zhou, D. Ma, S. Liu, W. Chen, S. Huang, *Nano-Micro Lett.* 7 (2015) 183–193.
- [24] Q. Zheng, B. Zhou, J. Bai, L. Li, Z. Jin, J. Zhang, J. Li, Y. Liu, W. Cai, X. Zhu, *Adv. Mater.* 20 (2008) 1044–1049.
- [25] H. Chen, J. Zhang, Q. Chen, J. Li, C. Dong, Y. Liu, B. Zhou, S. Shang, W. Cai, *Anal. Methods* 4 (2012) 1790–1796.
- [26] Q. Jiaa, K. Iwashinaa, A. Kudo, *Pros. Natl. Acad. Sci. U. S. A.* 109 (2012) 11564–11569.
- [27] D.K. Ma, M.L. Guan, S.S. Liu, Y.Q. Zhang, C.W. Zhang, Y.X. He, S.M. Huang, *Dalton Trans.* 41 (2012) 5581–5586.
- [28] N. Myung, S. Ham, S. Choi, W.G. Kim, Y.J. Jeon, K.J. Paeng, W. Chanmanee, N.R. Tacconi, K. Rajeshwar, *J. Phys. Chem. C* 115 (2011) 7793–7800.
- [29] Q. Zeng, J. Bai, J. Li, L. Xia, X. Li, B. Zhou, *J. Mater. Chem. A* 3 (2015) 4345–4353.
- [30] A.A. Tahir, K.G.U. Wijayantha, S. Saremi-Yarahmadi, M. Mazhar, V. McKee, *Chem. Mater.* 21 (2009) 3763–3772.
- [31] H.S. Casalongue, S. Kaya, V. Viswanathan, D.J. Miller, D. Friebe, H.A. Hansen, J.K. Nørskov, A. Nilsson, H. Ogasawara, *Nat. Commun.* 4 (2013) 2817–2822.

- [32] M.F. Al-Kuhaili, M. Saleem, S.M.A. Durrani, *J. Alloys Compd.* 521 (2012) 178–182.
- [33] K. Ji, H. Arandiyani, P. Liu, L. Zhang, J. Han, Y. Xue, J. Hou, H. Dai, *Nano Energy* 27 (2016) 515–525.
- [34] L. Xia, J. Bai, J. Li, Q. Zeng, X. Li, B. Zhou, *Appl. Catal. B: Environ.* 183 (2016) 224–230.
- [35] X. Chang, T. Wang, P. Zhang, J. Zhang, A. Li, J. Gong, *J. Am. Chem. Soc.* 137 (2015) 8356–8359.
- [36] W. He, R. Wang, L. Zhang, J. Zhu, X. Xiang, F. Li, *J. Mater. Chem. A* 3 (2015) 17977–17982.
- [37] K. Ye, Z. Chai, J. Gu, X. Yu, C. Zhao, Y. Zhang, W. Mai, *Nano Energy* 18 (2015) 222–231.
- [38] E.S. Kim, H.J. Kang, G. Magesh, J.Y. Kim, J. Jang, J.S. Lee, *ACS Appl. Mater. Interfaces* 6 (2014) 17762–17769.